



HAL
open science

Element differentiation with a Hartmann- based X-ray phase imaging system

Ombeline de La Rochefoucauld, Ginevra Begani Provinciali, Alessia Cedola, Philip Cook, Francesca Di Lillo, Guillaume Dovillaire, Fabrice Harms, Mourad Idir, Xavier Levecq, Laura Oudjedi, et al.

► **To cite this version:**

Ombeline de La Rochefoucauld, Ginevra Begani Provinciali, Alessia Cedola, Philip Cook, Francesca Di Lillo, et al.. Element differentiation with a Hartmann- based X-ray phase imaging system. Non-destructive Testing and Evaluation, 2022, 37 (5), pp.707-720. 10.1080/10589759.2022.2095383 . hal-04253819

HAL Id: hal-04253819

<https://hal.science/hal-04253819>

Submitted on 6 Nov 2023

HAL is a multi-disciplinary open access archive for the deposit and dissemination of scientific research documents, whether they are published or not. The documents may come from teaching and research institutions in France or abroad, or from public or private research centers.

L'archive ouverte pluridisciplinaire **HAL**, est destinée au dépôt et à la diffusion de documents scientifiques de niveau recherche, publiés ou non, émanant des établissements d'enseignement et de recherche français ou étrangers, des laboratoires publics ou privés.

Element differentiation with a Hartmann- based X-ray phase imaging system

Ombeline de La Rochefoucauld, Ginevra Begani Provinciali, Alessia Cedola, Philip K. Cook, Francesca Di Lillo, Guillaume Dovillaire, Fabrice Harms, Mourad Idir, Xavier Levecq, Laura Oudjedi, Tan-Binh Phan, Martin Piponnier, Giuliana Tromba & Philippe Zeitoun

To cite this article: Ombeline de La Rochefoucauld, Ginevra Begani Provinciali, Alessia Cedola, Philip K. Cook, Francesca Di Lillo, Guillaume Dovillaire, Fabrice Harms, Mourad Idir, Xavier Levecq, Laura Oudjedi, Tan-Binh Phan, Martin Piponnier, Giuliana Tromba & Philippe Zeitoun (2022): Element differentiation with a Hartmann- based X-ray phase imaging system, *Nondestructive Testing and Evaluation*, DOI: [10.1080/10589759.2022.2095383](https://doi.org/10.1080/10589759.2022.2095383)

To link to this article: <https://doi.org/10.1080/10589759.2022.2095383>



© 2022 The Author(s). Published by Informa UK Limited, trading as Taylor & Francis Group.



Published online: 05 Jul 2022.



Submit your article to this journal [↗](#)



Article views: 266



View related articles [↗](#)



View Crossmark data [↗](#)

Element differentiation with a Hartmann- based X-ray phase imaging system

Ombeline de La Rochefoucauld^a, Ginevra Begani Provinciali^{b,c}, Alessia Cedola^c, Philip K. Cook^d, Francesca Di Lillo^e, Guillaume Dovillaire^a, Fabrice Harms^a, Mourad Idir^f, Xavier Levecq^a, Laura Oudjedi^a, Tan-Binh Phan^{a,b}, Martin Piponnier^a, Giuliana Tromba^e and Philippe Zeitoun^b

^aR&D department, Imagine Optic, Orsay, France; ^bUMR7639, ENSTA, CNRS, Institut Polytechnique de Paris, Laboratoire d'Optique Appliquée, Palaiseau, France; ^co Physics Department, Sapienza University of Rome/Institute of Nanotechnology-CNR, Rome, Italy; ^dBM05, European Synchrotron Radiation Facility, Grenoble, France; ^eSYRMEP, Elettra-Sincrotrone Trieste, Basovizza, Italy; ^fOptics & Metrology Group, National Synchrotron Light Source II, Brookhaven National Laboratory, Upton, NY, USA

ABSTRACT

Significant efforts are currently ongoing in X-ray imaging to provide multimodal imaging systems, targeting better sensitivity and specificity for both biomedical or non-destructive testing applications. Knowing the elemental composition of specific structures, such as breast microcalcifications in mammography, would help to differentiate malign and benign tumours. Standard X-ray Phase Contrast Imaging techniques provide only qualitative information on elements with similar absorption properties. However, their chemical composition can be determined from the measurement of the phase as it is directly related to the optical index of elemental materials. We will show new experimental results obtained with an X-ray phase imaging system based on a Hartmann mask. Early data treatment succeeded in retrieving both the real and imaginary parts of the refractive index. The system demonstrates the capability to discriminate materials based on elemental composition.

ARTICLE HISTORY

Received 14 January 2022
Accepted 23 June 2022

KEYWORDS

X-Ray; phase contrast imaging; Hartmann; wavefront sensing; chemical analysis

1. Introduction

X-ray imaging is an essential tool for non-invasive analysis of various samples, both for biomedical diagnosis and non-destructive testing (NDT) applications. X-ray imaging is commonly performed in two or three dimensions (2D or 3D), where the second option offers more detailed information on the sample.

When absorption properties are very similar between two parts of the same sample, it becomes difficult to distinguish them using X-ray absorption imaging. This problem arises also when using high energy X-rays that make the sample transparent. X-ray phase imaging is a possible solution as it favours the phase over the amplitude contribution. Indeed, whatever the photon energy is, a sample always modifies the phase of an incident wave. This beam's phase shift caused by the sample can be either measured directly using an X-ray phase imaging system or can be transformed with a phase-contrast X-ray

imaging system into variations in intensity that are then recorded by the detector. In the latter case, intrinsically, the phase and the intensity are then merged in a single characteristic requiring advanced data treatment [1].

There are three kinds of techniques related to phase or phase-contrast imaging. Although they might look close to each other, they have fundamental differences. They are reviewed in [2–5]. Below we give a short overview of the different techniques.

1.1 Interferometry

In interferometry, the incoming beam is separated into two beamlets. One will serve as a reference and the second (the probe beam) will go through the object. The two beams then interfere in the detector to create fringes corresponding to the phase shift caused by the sample. In 1965, Bonse and Hart [6] developed the first X-ray interferometer and thus the first X-ray phase imaging technique.

The full list of interferometers is too long to be given here, we may cite some of them like the crystal-based interferometers [6,7], the phase-shifting point-diffraction interferometers [8], the Michelson interferometers [9], the Talbot interferometers [10], Talbot-Lau interferometers [11,12] and so on.

1.2 Deflectometry

In deflectometry, one measures the deflection undergone by the beam passing through an object, in other words, the local wave vectors. By integration of the deflections, one obtains the phase map (modulo 2π). Here are some examples of X-ray deflectometers: Moiré [13], Hartmann [14–17], Shack-Hartmann [18–20]. The most recent deflectometry technique uses a pattern of speckles produced by a diffracting plate placed after the sample. Deflection induced by the sample leads to a displacement of the speckle pattern that can be directly used to measure the local phase shift [21,22].

1.3 Phase-contrast imaging

Phase-contrast imaging has been invented in order to increase the contrast of images of samples having low variation of absorption. It is based on transforming the deflection induced by the variation of index of refraction into variation of intensity in the recorded image. These techniques do not directly measure the deflection.

Several methods have been applied like 1) Schlieren that consists in blocking undeflected rays with a knife-edge [23], 2) free-propagation [2,24] where deflected rays superimposed with straight rays producing a peak of intensity and consequently a neighbour drop of intensity, 3) edge illumination [25–27] or coded aperture [28,29] consisting in placing an array of blockers near a pixelated detector to stop straight rays, 4) analyser-based imaging [30,31] which is another evolution of Schlieren that takes benefit of the narrow angular acceptance of diffraction crystal (so-called rocking-curve) to enhance the contrast of the images.

In the proceedings of the ICT 2020 [32] we showed an X-ray phase imaging system based on the use of a Hartmann mask and its relevant data treatment algorithm. The system provides absorption, deflection and phase images with a single acquisition. Here,

we present results showing the ability of our X-ray phase-imaging system at differentiating materials with slightly different chemical compositions. The capabilities of Hartmann-based X-ray phase imaging (HXPI) based on the technology of Hartmann X-ray wavefront sensors open new opportunities in non-destructive testing (NDT) and in particular in finding pollutants in food, concrete, or any material. We first validated our approach using synchrotron light, the next step being to transpose it to table-top sources, widely used for NDT.

2. Principle of Hartmann-based X-ray phase imaging and element differentiation

2.1 Interaction of X-rays with matter

The interaction of X-rays with matter, in the absence of scattering, can be fully described through the complex refractive index of the medium. For X-rays, it is common to write the complex refractive index, n , of any multi-element material as:

$$n = 1 - \delta + i\beta \quad (1)$$

with

$$\delta = \frac{r_e \lambda^2}{2\pi} \sum_i n_a^i f_1^i(\lambda) \quad (2)$$

$$\beta = \frac{r_e \lambda^2}{2\pi} \sum_i n_a^i f_2^i(\lambda) \quad (3)$$

and with r_e the classical electron radius, λ the X-ray wavelength, n_a^i the density of atoms of the species 'i'. f_1^i and f_2^i are the tabulated atomic scattering factors for the 'i' atoms.

Assuming straight propagation of X-rays inside a homogeneous medium of thickness d (no scattering and negligible refraction), the electric field at the exit of the medium is given by $E = E_o \exp(i \frac{2\pi}{\lambda} nd)$ which can be rewritten, using Equation (1) as:

$$E = E_o \exp(i \frac{2\pi}{\lambda} d) \exp(-i\phi) \exp(-\frac{2\pi}{\lambda} \beta d) \quad (4)$$

with E_o the electric field at the entrance of the medium and ϕ the phase:

$$\phi = \frac{2\pi}{\lambda} \delta d \quad (5)$$

The first exponential is a complex number, independent of the chemical composition of the medium. It is equivalent to the transmission of air measured over the same thickness, d , of the medium, air having a refractive index approximated to unity. The second exponential term in Equation (4) is a pure imaginary number that modifies the X-rays phase, while the third exponential term is a pure real number thus impacting the intensity of X-rays. At this step, it is worth remembering the classical Beer-Lambert law considers only the variation of X-ray intensities recorded before (I_o) and after (I) propagating inside the medium of thickness d :

$$I = I_0 e^{-\mu d} \quad (6)$$

with μ the linear absorption coefficient.

Since $I = \|E\|^2$, it becomes simple to link μ to β through:

$$\mu = \frac{4\pi\beta}{\lambda} \quad (7)$$

To differentiate chemical elements using X-ray phase imaging, it is interesting to observe that in Equations (2) and (3), δ and β depend on the chemical composition of the material through f_1^i, f_2^i and n_a^i . The system is not closed since there are three variables for two equations. However, our current purpose is not to extract f_1^i, f_2^i and n_a^i from measurements but only to differentiate elements and in particular to detect pollutants. Therefore, the medium under consideration can no longer be considered as homogeneous. Since δ and β have transverse spatial variations they can be written as $\delta(x;y)$ and $\beta(x;y)$.

Indeed, from the measured phase (ϕ) and transmission (I/I_0) of X-rays through a sample, we can get the direct and independent measurement of $\delta(x;y)$ and $\beta(x;y)$ using Equations (5), (6) and (7). This procedure will allow us to detect the presence of pollutant and will provide valuable information for chemical differentiation.

2.2. Principle of Hartmann X-ray phase imaging (HXPI)

In this section, we will show that HXPI is perfectly suited to measure independently δ and β and thus to differentiate chemical elements. It is a robust apparatus consisting of a hole array (also called mask) and a pixelated detector [15,33,34]. When an incident beam goes through the mask up to the detector, it projects the image of the mask onto the detector (Figure 1).

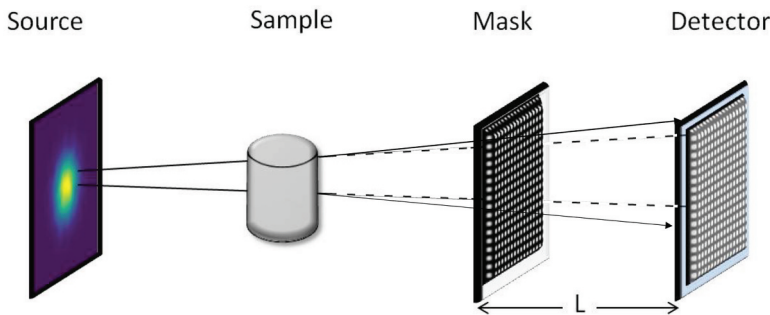


Figure 1. Schematic representation of the Hartmann X-ray imaging system: the Hartmann mask is placed in the beam path after the sample, between the source and the detector. L is the distance from the mask to the detector. The dotted lines show the X-ray paths without sample and the solid lines when the sample is inserted, thus deflecting the rays.

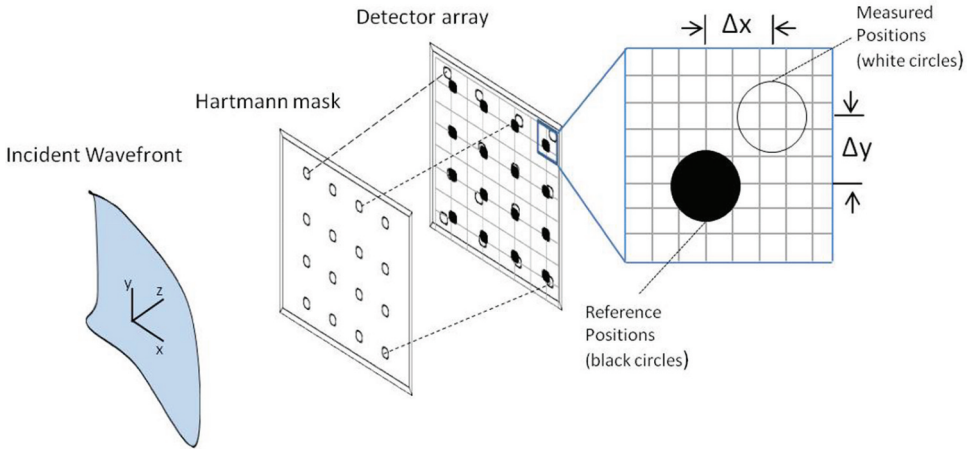


Figure 2. Drawing of the Hartmann X-ray phase imaging system, showing an incident wavefront traveling along the z-axis illuminating an aperture array and the spots generated on the detector and the displacement of a single spot from the reference location on the detector.

We acquire a reference image without sample and an image with the sample. Each hole in the Hartmann mask generates a bright spot on the camera. As illustrated [Figure 2](#), the shift of the measured spots with the sample (white spots) compared to the reference image without sample (black spots) is proportional to the deflection generated by the sample.

The vertical and horizontal shifts, x_{ij} and y_{ij} , respectively, are linked to the local derivatives of the phase $\phi(x,y)$ by:

$$\frac{\delta\phi}{\delta x} = \frac{\Delta x_{ij}}{L} \quad (8)$$

$$\frac{\delta\phi}{\delta y} = \frac{\Delta y_{ij}}{L} \quad (9)$$

with L the distance mask to the detector and i and j the row and column indexes, respectively.

For each hole, the difference between the two positions (with and without sample) gives the slope of the local phase through Equations (8), (9). This step generates two maps of the horizontal (x axis) and vertical (y axis) deflections of the incident beam after the sample. By integrating these two deflection maps, the phase induced by the sample is obtained. Finally, the ratio between the detector counts integrated over each spot with and without sample gives the local transmission. We thus obtained a fourth map displaying the sample transmission.

It is worth noting that in X-rays, the typical deflection value reaches few 10s of μrad or even smaller. Since it is important to keep the total length of the imaging system under a reasonable size (below or around 0.5 m), the required accuracy in finding the centroid of

each spot is challenging and requires sophisticated data treatment. There are numerous algorithms to detect centroids, as detailed in these theses [35,36]. This issue is at the heart of Imagine Optic software and remains a vivid field of improvement.

From two acquisitions (with and without sample) with the Hartmann-based X-ray imaging system, both transmission and phase maps of the sample are obtained simultaneously and independently. Knowing the sample thickness and using Equations (5) and (7), the transmission map might be easily transformed into $\mu(x,y)$ and $\beta(x,y)$, while $\delta(x,y)$ can be extracted from the phase map.

3. Demonstration of the chemical differentiation with a Hartmann-based X-ray phase imaging system

3.1 Context of the experiments

Our goal was to test the ability of HXPI system to distinguish samples of different chemical compositions from their δ and β . At the same time, we measured the phase and the transmission of different samples with similar chemical compositions, and then we retrieved δ and β . As presented in Equations (2) and (3), δ and β vary with the X-ray wavelength. However, table-top X-ray sources emit over very large spectra (bremsstrahlung) mixed with K or L emission lines. At a first glance, using such sources would lead to averaging δ and β over orders of magnitude, making such measurements worthless. Synchrotrons are the reference X-ray source for metrology since the spectrum is perfectly known and very stable as is their X-ray flux. Therefore, to validate our approach, we conducted a first experiment using a monochromatic beam at the ESRF synchrotron (section 3.2). We then increased the complexity of the experiment one step further by using a white beam with reduced bandwidth at the Elettra synchrotron (section 3.3).

For both experiments, we used a compact HXPI system developed by Imagine Optic (Figure 3). The system is ~ 50 cm in length, and has a clear aperture of about 3 mm in diameter. The Hartmann mask contains about 130×130 holes, i.e. measurement points. The spatial resolution of a HXPI system is given by the distance between two holes of the

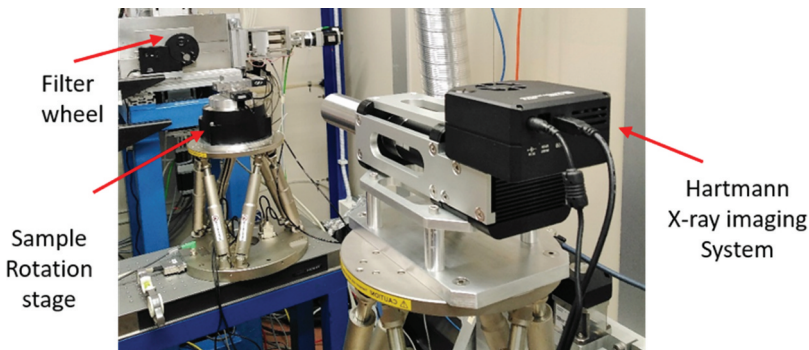


Figure 3. Picture of the experimental set-up installed at SYRMEP beamline of ELETTRA synchrotron illustrating the relative positions of the Hartmann X-ray imaging system and the sample rotation stage compared to the direction of the X-ray beam.

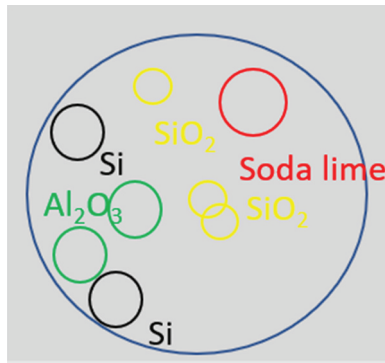


Figure 4. Scheme displaying the position of the eight spheres of different chemical compositions: yellow for SiO_2 , black for Si, green for Al_2O_3 and red for soda lime glass.

Table 1. Theoretical values of β and δ at 10, 12, 14, 16 and 22 keV for the different spheres calculated from the Center for X-Ray Optics website [37].

Theoretical values		Si	Al_2O_3	SiO_2	Soda lime
δ	10 keV	4.89×10^{-6}	8.15×10^{-6}	4.58×10^{-6}	4.6×10^{-6}
	12 keV	3.35×10^{-6}	5.6×10^{-6}	3.16×10^{-6}	3.14×10^{-6}
	14 keV	2.46×10^{-6}	4.11×10^{-6}	2.32×10^{-6}	2.31×10^{-6}
	16 keV	1.89×10^{-6}	3.15×10^{-6}	1.78×10^{-6}	1.77×10^{-6}
	22 keV	9.95×10^{-7}	1.66×10^{-6}	9.4×10^{-7}	9.35×10^{-7}
β	10 keV	7.38×10^{-8}	6.18×10^{-8}	3.91×10^{-8}	4.71×10^{-8}
	12 keV	3.53×10^{-8}	2.94×10^{-8}	1.86×10^{-8}	2.26×10^{-8}
	14 keV	1.92×10^{-8}	1.59×10^{-8}	1.01×10^{-8}	1.23×10^{-8}
	16 keV	1.14×10^{-8}	9.45×10^{-9}	6.01×10^{-9}	7.34×10^{-9}
	22 keV	3.29×10^{-9}	2.73×10^{-9}	1.73×10^{-9}	2.12×10^{-9}

mask. In a cone beam configuration, one can adjust the distance between the sample and the mask to get better spatial resolution but with the tradeoff of reducing the field of view. A full description of the HXPI system can be found in [32,33].

For both experiments, we tested the same samples composed of small spheres (Figure 4) made of high-purity silicon (Si), silicon oxide (SiO_2), alumina (Al_2O_3) and soda lime glass ($\text{Si}_{70}\text{O}_{172}\text{Na}_{30}\text{Ca}_{10}\text{MgB}_2\text{Al}_2$). These spheres have been chosen since their chemical composition and average atomic numbers $\langle Z \rangle$ are close to each other: 14 for Si, 10 for SiO_2 and Al_2O_3 and for 10.2 for soda lime. The diameters of the spheres were of $480 \mu\text{m}$ for Si, $500 \mu\text{m}$ for Al_2O_3 , $350 \mu\text{m}$ for SiO_2 and $700 \mu\text{m}$ for soda lime. Table 1 assembles the theoretical β and δ values of the spheres at different energies to illustrate the similarity of their composition.

3.2 Monochromatic measurements at ESRF

The monochromatic experiment has been performed on the BM05 beamline of European Synchrotron Radiation Facility (ESRF, France) at three different energies: 10 keV, 12 keV and 14 keV in a parallel beam configuration.

From the images with and without sample, four maps (transmission, horizontal and vertical deflections, and the phase) could be measured. Deflections are expressed in radian and phase in nm, which corresponds to the differential optical path due to the X-ray passing through the object compared to the reference image (i.e. phase multiplied by the wavelength/ 2π). The images acquired at 12 keV are shown in Figure 5. It is difficult to differentiate Si (black) and Al_2O_3 (green) spheres from the transmission map, while they present a different phase signal: phase of the Al_2O_3 spheres is darker (higher) than for Si.

From the values of Table 1, it means that our system does not allow us to differentiate elements with a variation of β of 0.59×10^{-8} but we can differentiate δ of 2.25×10^{-6} . Transmission and phase maps of both Al_2O_3 (green) and soda lime (red) spheres are very similar at 12 keV. Our system is not able to separate them. On the contrary, Si (black) and SiO_2 (yellow) look different on the transmission map (the difference in β is 1.67×10^{-8}), with lower transmission for Si than SiO_2 (higher β for Si and SiO_2) while more similar on the phase (small difference in δ of 0.19×10^{-6}). These first results are purely qualitative.

SiO_2 and soda lime have similar δ at 12 keV (3.16 and 3.14×10^{-6}), but the phase of the soda lime is higher, as this sphere is larger (Figure 5). This effect is also visible where there is the superposition of the two SiO_2 spheres: the thickness is greater; the phase image is darker. Comparing contrast on the phase and transmission maps is not enough to differentiate elements of different sizes.

Using the HPXI system we can calculate the transmission and phase maps. Knowing the sphere thickness, it is possible, using Equation (5-7), to measure experimentally β and δ for the different spheres at the different energies (10, 12 and 14 keV). Results have been reported in the graphs in Figure 6. The experimental results (red dots) were compared with the tabulated index of refraction for compound materials available online on the Center for X-Ray Optics website [37] (blue crosses). They fit well with less than 10% error.

It is worth noting that the δ for Si and SiO_2 at these energies are very similar (difference of 0.3×10^{-6} at 10 keV, 0.2×10^{-6} at 12 keV and 0.14×10^{-6} at 14 keV), making it impossible to differentiate them on the basis of delta knowledge alone. On the other hand, the β values are sufficiently different (difference of 3.47×10^{-8} at 10 keV, 1.67×10^{-8} at 12 keV and 0.91×10^{-8} at 14 keV). Our ability to independantly calculate both δ and β at a few energies allows us to distinguish Si from SiO_2 .

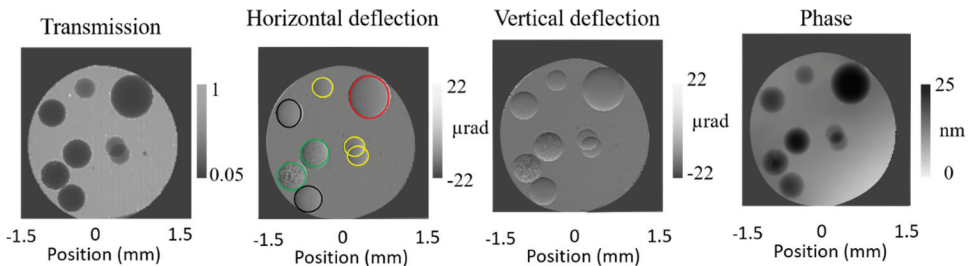


Figure 5. False color maps of the transmission, horizontal and vertical deflection, and phase measured at 12 keV for the set of 8 spheres: yellow for SiO_2 , black for Si, green for Al_2O_3 and red for soda lime glass.

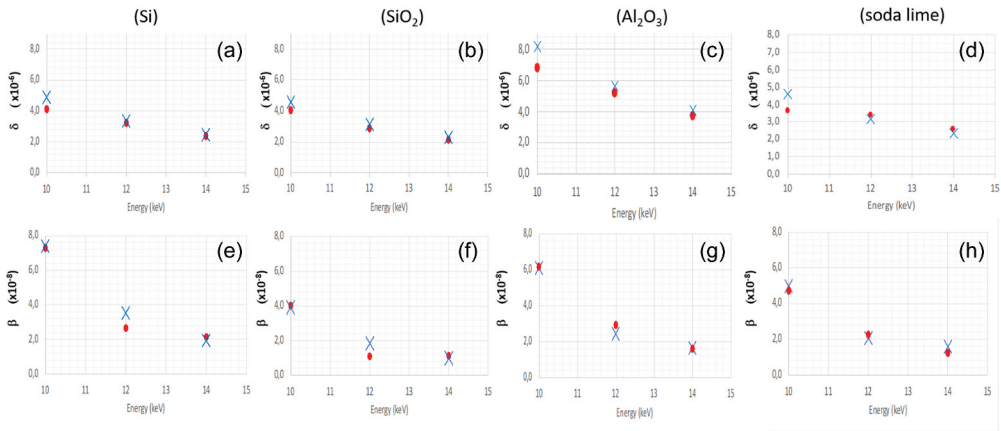


Figure 6. Comparison of experimental values (red dot) of δ versus theoretical ones (crosses) for Si (A), SiO₂ (B), Al₂O₃ (C) and soda lime (D) and β for Si (E), SiO₂ (F), Al₂O₃ (G) and soda lime (H). The vertical error bars have not been displayed since they are of few per cent and would not be visible.

Another example is given by the value of β for SiO₂ (3.91×10^{-8}) and Al₂O₃ (6.18×10^{-8}) that are easily differentiable at 10 keV but become much closer at 14 keV (SiO₂: 1.01×10^{-8} ; Al₂O₃: 1.59×10^{-8}) making their separation more challenging. However, the values of δ at 14 keV are quite different for SiO₂ (2.32×10^{-6}) and Al₂O₃ (4.11×10^{-6}): difference of 1.79×10^{-6} . The knowledge of both δ and β at a few energies allows us to confirm the initial guess based on β values at 10 keV.

These examples show that the ability to directly and independently measure δ and β on a single acquisition with the HXPI is a key advantage for chemical differentiation.

3.3 Polychromatic measurements at Elettra synchrotron

In order to mimic table-top sources, we measured the real and imaginary parts of the index of refraction of the same samples but using standard ‘pink-beam’ [38–40]. The experiment has been performed at the SYRMEP beamline of the ELETTRA synchrotron (Italy). The HXPI system was set at about 20 cm from the sample (Figure 3). The parallel X-ray beam covered the full sensor aperture.

The X-ray spectrum available at SYRMEP beamline extends over a very large set of energies from a few keV up to 50 keV. In order to reduce the spectral width, we placed a set of specially designed filters before the sample. A 2 mm beryllium filter is permanently installed on the beamline as a window between vacuum and air and had to be taken into account in the filter calculation. We present results obtained with four different home-made filters defined by their central energy (and bandwidth): ~ 16 keV ± 1 keV, 17.6 keV ± 0.6 keV, 20.5 keV ± 3.2 keV and 22.6 keV ± 3.2 keV.

The images acquired for the same sample described in Figure 4 are shown in Figure 7: the transmission (Figure 7(a)), the deflections in the X and Y directions (Figure 7(b–c) respectively) and the reconstructed phase (Figure 7(d)). Results were obtained for two different incident spectra: one centred around 16 keV (upper row in Figure 7) and the second one at 22 keV (lower row in Figure 7).

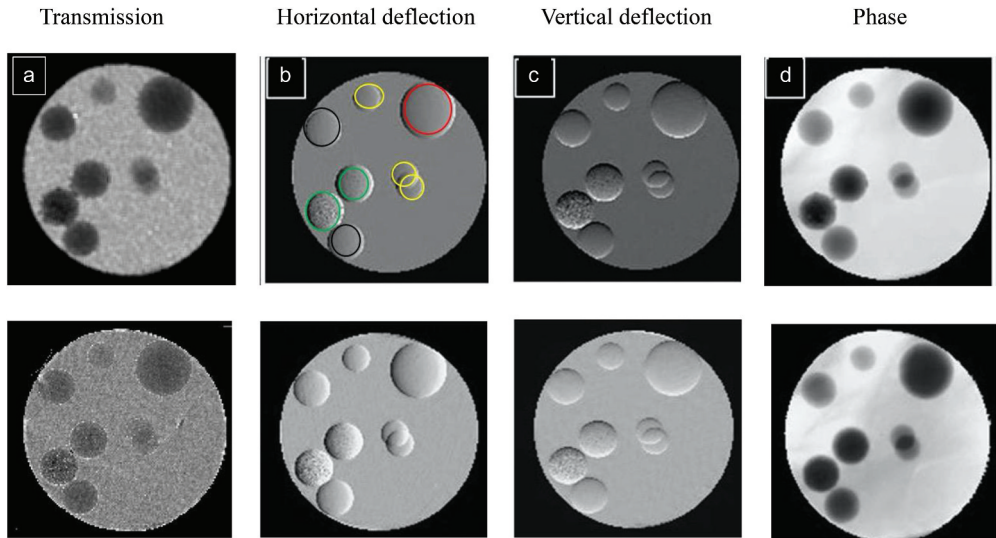


Figure 7. Transmission, horizontal deflections, vertical deflections and phase reconstruction. The upper row corresponds to a mean energy of 16 keV, while the bottom row corresponds to 22 keV. The color code is used to differentiate the 4 kinds of spheres: soda lime in red, Al_2O_3 in green, Si in black and SiO_2 in yellow.

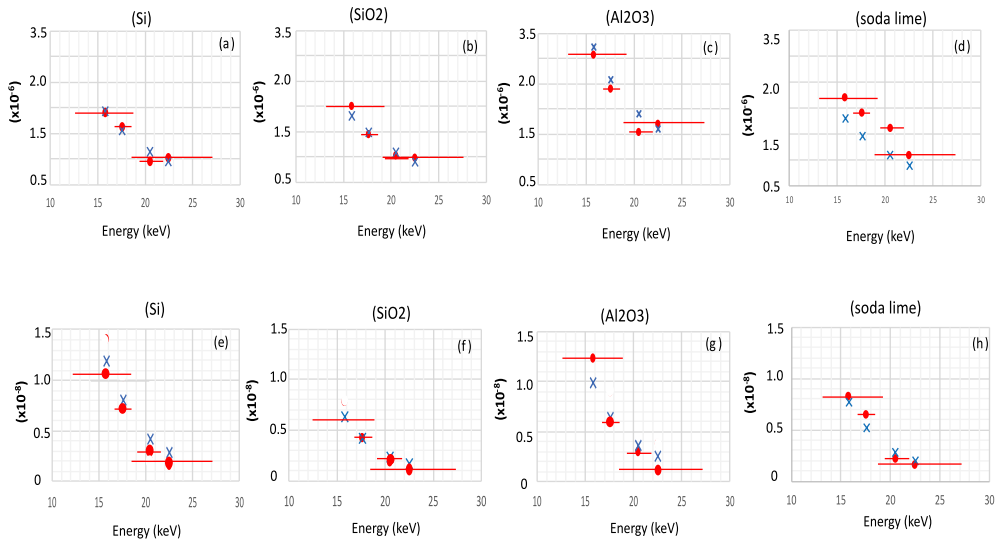


Figure 8. Variation of δ (top row) and β (bottom row) for Si (a and e), SiO_2 (b and f), Al_2O_3 (c and g) and soda lime (d and h) versus X-ray energies. Theoretical values are displayed with blue crosses fitted together to show the trend. Experimental values are shown as red dots with red bars giving the spectral width of the individual filter used. The experimental points are placed at the mean energy of each filter.

As the energy increases, the photon-noise increases and all the spheres start to be transparent to X-rays resulting in a reduced contrast: from 0.5 at 16keV to 0.19 at 22 keV for the soda lime, from 0.48 to 0.18 for Si, from 0.55 to 0.2 for Al_2O_3 and from 0.2 to 0.04 for the SiO_2 spheres, using the classical formula $(I_{\text{max}} - I_{\text{min}})/(I_{\text{max}} + I_{\text{min}})$.

At 22 keV, it is difficult to differentiate the soda lime (red), Al_2O_3 (green) and silicon (black) spheres from the absorption map, as the β values are all within 1.56×10^{-9} , while we can easily differentiate the Al_2O_3 (green) from the silicon (black) spheres on the phase map (all the δ values are within 7.25×10^{-7}).

Figure 8 displays the measurements as well as theoretical values of δ (a to d) and β (e to h) for pure Si (a and e), SiO_2 (b and f), Al_2O_3 (c and g) and soda lime (d and h) for four different spectral ranges corresponding to four homemade filters. In general, the experimental values (red dots) agree well with theoretical ones (blue crosses), demonstrating efficiency for chemical discrimination of the reduction of spectral width using a combination of broad band X-ray source (few keV) and homemade filter.

4. Conclusion

In this article, we have shown our ability to distinguish known elements of different chemical composition using Hartmann X-ray phase imaging. This device has the key ability to measure in 2D, directly and on a single acquisition the absorption, the X-ray horizontal and vertical deflections and the phase. The method has been validated first on a monochromatic beam, then on a polychromatic X-ray beam with a spectrum of few keV, both on a synchrotron facilities. The use of special filters was necessary to ensure a reliable measurement while using polychromatic X-rays that correspond to the emission of a table-top X-ray source. Measurements of β and δ at a few energies are needed to ensure a high degree of confidence. The next step will be to reproduce this experiment on a tabletop X-ray source and to show our ability to differentiate truly unknown materials using a tabletop experiment. Although this work shows promising results for chemical differentiation, several improvements have to be made in order to retrieve the exact chemical composition of unknown specimens.

Acknowledgement

This research was funded by the 3DX-LIGHT project (European Union's Horizon 2020 research and innovation programme) under grant agreement n° 851956, by the XPulse project (Région Nouvelle-Aquitaine and the European Union FEDER, FEDER/FSE Aquitaine 2014–2020), grant agreement n°3334910, by LASERLAB-Europe Joint Research Activity grant agreement n°871124, by PLENO-X supported by Investissements d'Avenir from LabEx PALM (ANR-10-LABX-0039-PALM), IMREX from CNRS under Prematuration 2021 funding and the support of Prematuration 2019 project (VOXEL-PREMAT) from IP Paris. MI gratefully acknowledges the support of the Accelerator and Detector Research Programme, part of the Scientific User Facility Division of the Basic Energy Science Office of the U.S. Department of Energy, under the project 'Wavefront Preserving Mirrors'. The FISR Project 'Tecnopolo di nanotecnologia e fotonica per la medicina di precisione' (funded by MIUR/CNR, CUP B83B17000010001) and the TECNOMED project (funded by Regione Puglia, CUP B84I18000540002) are also acknowledged.

We acknowledge all the team at SYRMEP (Elettra) beamline for providing us access to their beamlines and for their technical support. We acknowledge the European Synchrotron Radiation Facility for provision of synchrotron radiation facilities, and we would like to thank all the team of beamline BM05 for assistance.

Disclosure statement

No potential conflict of interest was reported by the author(s).

Funding

The work was supported by the Conseil Régional Nouvelle-Aquitaine [3334910]; Horizon 2020 Framework Programme [851956]; MIUR/CNR [CUPB83B17000010001]; IP Paris [VOXEL-PREMAT]; Laserlab-Europe [871124]; Regione Puglia [CUP B84I18000540002]; Investissements d'Avenir from LabEx PALM [PLENO-X]; CNRS under Prematuration 2021 [IMREX]; Scientific User Facility Division of the Basic Energy Science Office of the U.S. Department of Energy [Wavefront Preserving Mirrors].

References

- [1] Chen RC, Rigon L, Longo R. Comparison of single distance phase retrieval algorithms by considering different object composition and the effect of statistical and structural noise. *Opt Express*. 2013;21(6):7384.
- [2] Bravin A, Coan P, Suortti P. X-ray phase-contrast imaging: from pre-clinical applications towards clinics. *Phys Med Biol*. 2013;58(1):R1–R35.
- [3] Auweter SD, Herzen J, Willner M, et al. X-ray phase-contrast imaging of the breast—advances towards clinical implementation. *Br J Radiol*. 2014;87(1034):20130606.
- [4] Wilkins SW, Nesterets YI, Gureyev TE, et al. On the evolution and relative merits of hard X-ray phase-contrast imaging methods. *Philos Trans R Soc a Math Phys Eng Sci*. 2014;372(2010):20130021.
- [5] Momose A, Takano H, Wu Y, et al. Recent progress in X-ray and neutron phase imaging with gratings. *Quantum Beam Sci*. 2020;4(1):9.
- [6] Bonse U, Hart M. An x-ray interferometer. *Appl Phys Lett*. 1965;6(8):155–156.
- [7] Momose A. Demonstration of phase-contrast X-ray computed tomography using an X-ray interferometer. *Nucl Instrum Methods Phys Res a*. 1995;352(3):622–628.
- [8] Goldberg KA. Progress towards $\lambda/20$ extreme ultraviolet interferometry. *J Vac Sci Technol B: Microelectron Nanometer Struct*. 1995;13(6):2923.
- [9] Smith RF, Dunn J, Hunter JR, et al. Longitudinal coherence measurements of a transient collisional x-ray laser. *Opt Lett*. 2003;28(22):2261.
- [10] Momose A, Kawamoto S, Koyama I, et al. Demonstration of X-ray talbot interferometry. *Jpn J Appl Phys*. 2003;42(Part 2, No. 7B):L866–L868.
- [11] Weitkamp T, Nöhammer B, Diaz A, et al. X-Ray wavefront analysis and optics characterization with a grating interferometer. *Appl Phys Lett*. 2005;86(5):054101.
- [12] Pfeiffer F, Weitkamp T, Bunk O, et al. Phase retrieval and differential phase-contrast imaging with low-brilliance X-ray sources. *Nat Phys*. 2006;2(4):258–261.
- [13] Röss D, DaSilva LB, London RA, et al. Measurement of laser-plasma electron density with a soft X-ray laser deflectometer. *Sci*. 1994;265(5171):514–517.
- [14] Wilkins SW. Improved x-ray optics, especially for phase contrast imaging. WO 95/05725. 1995.
- [15] Mercère P, Zeitoun P, Idir M, et al. Hartmann wave-front measurement at 13.4 nm with λ -EUV/120 accuracy. *Opt Lett*. 2003;28(17):1534.

- [16] Krejci F, Jakubek J, Kroupa M. Hard X-ray phase contrast imaging using single absorption grating and hybrid semiconductor pixel detector. *Rev Sci Instrum.* **2010**;81(11):113702.
- [17] Hildebrand M, Leck M, Gudat J. Three-dimensional X-ray phase imaging of impact damaged carbon-fiber- reinforced polymers by using a pinhole array. In 8th Conference on Industrial Computed Tomography; Wels, Austria; **2018**. (iCT 2018).
- [18] Le Pape S, Zeitoun P, Idir M, et al. Electromagnetic-Field distribution measurements in the soft X-ray range: full characterization of a soft X-ray laser beam. *Phys Rev Lett.* **2002**;88(18):1839011–1839014.
- [19] dos Santos Rolo T, Reich S, Karpov D, et al. A Shack-Hartmann sensor for single-shot multi-contrast imaging with hard X-rays. *Appl Sci.* **2018**;8(5):737.
- [20] Mikhaylov A, Reich S, Zakharova M, et al. Shack–Hartmann wavefront sensors based on 2D refractive lens arrays and super-resolution multi-contrast X-ray imaging. *J Synchrotron Radiat.* **2020**;27(3):788–795.
- [21] Berujon S, Wang H, Sawhney K. X-Ray multimodal imaging using a random-phase object. *Phys Rev a.* **2012**;86(6):063813.
- [22] Zdora M-C. State of the art of X-ray speckle-based phase-contrast and dark-field imaging. *J Imaging.* **2018**;4(5):60.
- [23] Watanabe N, Sasaya T, Imai Y, et al. Obs phase objects by using an X-ray microscope with a Foucault knife-edge. **2011**; pp. 313–316. [10.1063/1.3625367](https://doi.org/10.1063/1.3625367)
- [24] Snigirev A, Snigireva I, Kohn V, et al. On the possibilities of X-ray phase contrast micro-imaging by coherent high-energy synchrotron radiation. *Rev Sci Instrum.* **1995**;66(12):5486–5492.
- [25] Olivo A, Arfelli F, Cantatore G, et al. An innovative digital imaging set-up allowing a low-dose approach to phase contrast applications in the medical field. *Med Phys.* **2001**;28(8):1610–1619.
- [26] Diemoz PC, Endrizzi M, Zapata CE, et al. X-Ray phase-contrast imaging with nanoradian angular resolution. *Phys Rev Lett.* **2013**;110(13):138105.
- [27] Olivo A. Edge-Illumination x-ray phase-contrast imaging. *J Phys.* **2021**;33(36):363002.
- [28] Olivo A, Speller R. A coded-aperture technique allowing x-ray phase contrast imaging with conventional sources. *Appl Phys Lett.* **2007**;91(7):074106.
- [29] Kallon GK, Wesolowski M, Vittoria FA, et al. A laboratory based edge-illumination x-ray phase-contrast imaging setup with two-directional sensitivity. *Appl Phys Lett.* **2015**;107(20):204105.
- [30] Förster E, Goetz K, and Zaumseil P. Double crystal diffractometry for the characterization of targets for laser fusion experiments. *Kristall und Technik.* **1980**;15(8):937–945. <https://doi.org/10.1002/crat.19800150812>
- [31] Davis TJ, Gao D, and Gureyev TE, et al. Phase-Contrast imaging of weakly absorbing materials using hard X-rays letters to nature. *Nat.* **1995**;373:595–598.
- [32] de La Rochefoucauld O, Provinciali GB, Cedola A, et al. Single-Shot, high sensitivity X-ray phase contrast imaging system based on a Hartmann mask. In 10th Conference on Industrial Computed Tomography (iCT) 2020; Feb, Wels, Austria; **2020**. p. 4–7. (iCT 2020).
- [33] de La Rochefoucauld O, Dovillaire G, Harms F, et al. EUV and hard X-ray Hartmann wavefront sensing for optical metrology, alignment and phase imaging. *Sens.* **2021**;21(3):874.
- [34] Li L, Koliyadu JCP, Donnelly H, et al. High numerical aperture Hartmann wave front sensor for extreme ultraviolet spectral range. *Opt Lett.* **2020**;45(15):4248.
- [35] Roman Ferstl. Optimised centroiding of stars for space applications. University Vienna. **2016**. DOI: [10.25365/thesis.41269](https://doi.org/10.25365/thesis.41269)
- [36] Begani Provinciali G. X-Ray phase imaging based on Hartmann wavefront sensor for applications on the study of neurodegenerative diseases. Palaiseau, France: Institut Polytechnique de Paris; **2022**.

- [37] Henke BL, Gullikson EM, Davis JC. X-Ray interactions: photoabsorption, scattering, transmission, and reflection at $E = 50\text{-}30,000$ eV, $Z = 1\text{-}92$. At Data Nucl Data Tables. 1993;54(2):181–342.
- [38] Marathe S, Storm M, Kuppilli VSC, et al. Development of synchrotron pink beam x-ray grating interferometer at the diamond light source I13-2 beamline. In: Müller B & Wang G, editors. Developments in X-Ray tomography XII. SPIE; 2019. p. 42. DOI:[10.1117/12.2530698](https://doi.org/10.1117/12.2530698).
- [39] Rivers M. Synchrotron ‘pink beam’ tomography for the study of dynamic processes. SPIE Newsroom. 2016. DOI:[10.1117/2.1201608.006674](https://doi.org/10.1117/2.1201608.006674)
- [40] Mittone A, Fardin L, Di Lillo F, et al. Multiscale pink-beam microCT imaging at the ESRF-ID17 biomedical beamline. J Synchrotron Radiat. 2020;27(5):1347–1357.